Materials & Design 268 (2026) 116517

Contents lists available at ScienceDirect

Materials & Design

journal homepage: www.elsevier.com/locate/matdes

Compositional tuning of structural, photothermal and optical properties of La-based high-entropy perovskite oxides

Anurag Khandelwal [a], Piyush Anil Kumar Sharma [a], Simon Schweidler [a], Pirmin Tischler [b], Uli Lemmer [b], Holger Röhm [b,c], Alexander Colsmann [b,c,*], Jasmin Aghassi-Hagmann [a], Ben Breitung [a,*]

[a] Institute of Nanotechnology, Karlsruhe Institute of Technology, Kaiserstraße 12, 76131 Karlsruhe, Germany
[b] Light Technology Institute, Karlsruhe Institute of Technology, Kaiserstraße 12, 76131 Karlsruhe, Germany
[c] Material Research Center for Energy Systems, Karlsruhe Institute of Technology, Kaiserstraße 12, 76131 Karlsruhe, Germany

ARTICLE INFO

Keywords:
High-entropy oxides
Perovskites
Structural properties
Optical properties
Photoluminescence

ABSTRACT

In this study, 14 lanthanum-based high-entropy perovskite oxides (HEPOs) with equimolar mixtures of transition metals (Cr, Mn, Fe, Co, Ni, Cu, Zn) at the B-site were synthesized to investigate how multi-elemental interactions govern their structural and optical properties. Most compositions form single-phase perovskites after annealing at 1200 °C, as confirmed by XRD and Rietveld refinement. SEM and EDS reveal homogeneous elemental distributions with particle sizes tunable from < 250 nm to > 2 μm depending on composition. UV–Vis-NIR spectrometry shows broad absorption without a distinct measurable onset, while the electronic structure remains robust across the series. Ionisation potentials shift by up to 0.55 eV with cationic composition, demonstrating systematic compositional tuning of the occupied band (analogous to the valence band maximum). Photoluminescence measurements indicate thermally driven emission resembling broadband thermal radiation, consistent with a strong photothermal response in these materials. These results highlight high-entropy perovskite oxides as a versatile platform for engineering structural disorder, electronic energy-level alignment, and photothermal behavior, opening pathways toward oxide-based broadband infrared emission and high-temperature photothermal applications.

Introduction

High-entropy materials (HEMs) represent an exciting approach to synthesizing new materials, emerging from the pioneering work on high-entropy alloys.[1,2] They stand out due to their unique compositions, which typically involve the incorporation of five or more elements in near-equimolar ratios at the same site of the (sub)lattice. This diversity in elemental composition leads to a remarkable range of physical and chemical properties that often surpass those of traditional binary or ternary materials, owing to so-called cocktail effects and lattice distortions.[3–6] The interactions between the incorporated elements determine the properties of the materials and can be harnessed to fine-tune these properties by substituting elements or adjusting the stoichiometry.[7,8] Beyond their expanding use in energy storage[9], memristive devices[10], and catalysis[11], HEMs offer unprecedented freedom in tailoring electronic structure, an aspect particularly relevant for optoelectronic applications.[12] The exploration of HEMs not only paves the way for the development of advanced functional systems but also provides deeper insight into elemental interactions for material design.

Perovskite structures, i.e., crystals with the generic formula ABX_3 (where 'A' and 'B' are cations and 'X' is an anion, in this case oxygen), are well-known for their versatile physical and chemical properties, which can include superconductivity, ferroelectricity, magnetoresistivity, and ionic conductivity.[13–16] By incorporating high-entropy strategies into perovskite oxides, researchers have synthesized materials that not only retain these desirable properties but also exhibit enhanced stability and novel functionalities, thereby offering a promising avenue for discovering new materials for applications spanning multiple scientific and engineering domains.[17] With the growing need for sustainable materials, high-entropy perovskite oxides (HEPOs) have attracted considerable interest in the context of photovoltaic research, particularly as potential alternatives to lead-based compounds.[18,19] The judicious selection of constituent cations has been proposed as a route to modify their electronic landscapes, optical absorption characteristics,

* Corresponding authors.

https://doi.org/10.1016/j.matdes.2026.116517
Received 18 May 2026; Received in revised form 18 June 2026; Accepted 25 June 2026
Available online 3 July 2026

including the absorption edge, and to influence defect formation energies and recombination pathways.[20–23] The increased structural and chemical stability of HEOs has been suggested as a potential advantage for long-term operation in solar-energy-related environments.[13,24–26] In the following, absorption refers to photothermal light–matter interaction, i.e., the efficient conversion of incident radiation into heat, rather than carrier-generating absorption as required for photovoltaic devices.

In this study, a sol–gel synthesis technique, the modified Pechini process, which employs citric acid and ethylene glycol for the chelation and esterification of the precursors, has been used to prepare a series of high-entropy perovskite-structured oxides.[27–29] This resulted in 14 different lanthanum-based HEPO powders, in which an equimolar mixture of transition metals occupies the B-site, laying the foundation for the production of pellets or thin films thereof. La-based perovskite systems, such as La_2NiMnO_6, $LaFe_{0.9}Zn_{0.1}O_3$, and $LaMnO_3$, have been explored as absorber layers for solar cells due to their smaller band gaps (1.6–1.8 eV), which show good ambient stability and light absorption.[30–32] In contrast to binary $LaBO_3$ perovskites, introducing high configurational entropy at the B-site provides an additional degree of freedom for engineering band structure, defect populations, and light absorption. This makes La-based HEPOs a promising platform for systematic optical and photothermal tuning. Previous studies on optical or photothermal high-entropy oxides have mostly focused on individual compositions, thin films, or device-oriented absorber concepts, whereas systematic correlations between defined B-site cation selection, phase stability, ionisation potential, broadband absorption, and photothermal response remain scarce. In this work, we therefore use a composition series of fourteen La-based HEPOs with equimolar five-cation B-site configurations selected from Cr, Mn, Fe, Co, Ni, Cu, and Zn. This allows us to identify how specific cations, particularly Cu and Zn, influence perovskite phase stability, energy-level alignment, particle morphology, and broadband optical/photothermal behavior. The study thus provides composition–structure–property relationships for La-based HEPOs as compositionally tunable broadband photothermal oxide systems.

Results and Discussion

In this study, we focus on the synthesis and characterization of lanthanum oxides with perovskite structure ($LaBO_3$), where the B-site is occupied by an equimolar mixture of five transition metals chosen from Cr, Mn, Fe, Co, Ni, Cu, and Zn. To investigate their suitability for optical applications, we sought to tune their electronic structure by varying the B-site composition, as the B-site cation strongly influences the distribution and hybridization of electronic states in perovskites.[33] The transition metals were selected for this study because they possess broadly comparable ionic radii and form $LaBO_3$-type perovskites in many binary systems, thereby minimizing the risk of phase separation during synthesis. In addition, most form binary or ternary perovskites with La. Since these selected transition metals can exhibit multiple valence states, charge neutrality can be maintained even in the presence of vacancies. All these factors together support the formation of a single-phase high-entropy oxide.[34]

Crystal Structure.

In an idealized perovskite system with a cubic structure, the B-site cations form the BO_6 octahedra alongside the oxygen anions, thereby creating a three-dimensional network in which the A-site cations occupy the cuboctahedral voids (Fig. 1**a**). However, due to distortions arising from variations in cation sizes and electronegativities, the crystal structure may adopt different crystallographic symmetries, such as rhombohedral, orthorhombic, tetragonal, and hexagonal. In particular, smaller A-site cations promote the formation of either an orthorhombic or rhombohedral configuration. The parent lanthanum perovskite oxides of transition metals demonstrate either an orthorhombic structure (*Pnma*; for $LaCrO_3$, $LaMnO_3$, and $LaFeO_3$) or a rhombohedral structure (*R*-3*cH*; for $LaNiO_3$, $LaCoO_3$, and $LaCuO_3$). $LaZnO_3$ stands out as an outlier with a hexagonal structure ($P6_3mc$).[35] An orthorhombic and a rhombohedral structure are visualized in Fig. 1**b** and Fig. 1**c**, respectively.

The structural stability of perovskites can also be predicted using geometric descriptors. The Goldschmidt tolerance factor t in **Equation (1)** estimates how well the A-site cation fits in the voids between corner-sharing BO_6 octahedra.[36]

$$t = \frac{r_A + r_O}{\sqrt{2}(r_B + r_O)} \tag{1}$$

r_A is the radius of the A cation, r_B is the radius of the B cation, and r_O is the radius of the anion (oxygen in the case of these perovskites). Compositions having $0.7 < t < 1$ tend to crystallise in an orthorhombic or a rhombohedral structure, which, in this study, is in good agreement with the diffraction analysis below.

Another descriptor for the stability of a perovskite phase is the octahedral factor μ, which is the ratio of the r_B to r_O.[37] μ describes the fitting of the B-site cation into the center of the octahedron formed by the anions. BO_6 octahedra are commonly formed if $0.414 < \mu < 0.732$. If $\mu > 0.732$, the B-cation is too large for proper coordination, and if $\mu < 0.414$, the B-cation is too small, resulting in an unstable octahedron. Recently, Bartel et al. proposed a revised tolerance factor τ for predicting the stability of perovskite structures with higher accuracy, which also takes the oxidation state of the A-site n_A into account. This oxidation-state-weighted tolerance factor is described by **Equation (2)**. $\tau < 4.18$ indicates that a perovskite structure is likely to form. The geometric

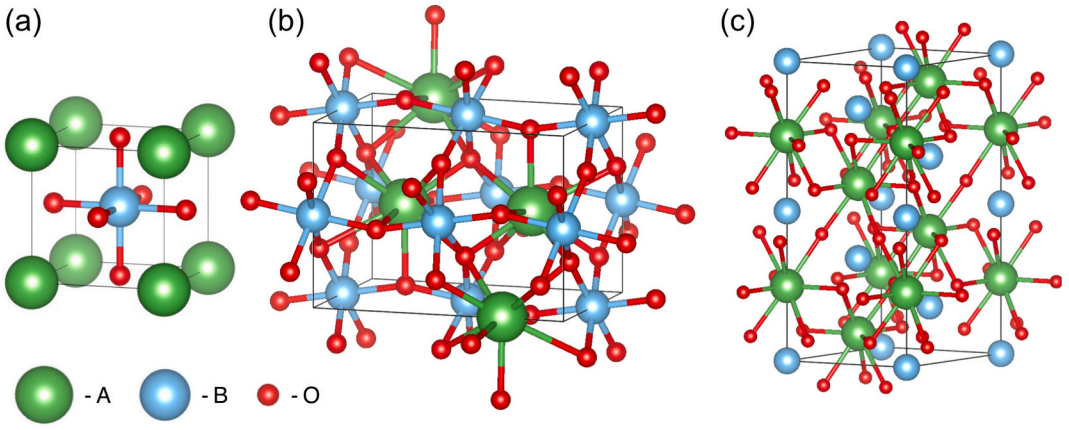

Fig. 1. (a) Unit cell of an ideal cubic perovskite oxide crystal, ABO_3. (b) The orthorhombic crystal structure of a perovskite oxide, e.g. $LaCrO_3$. (c) The rhombohedral crystal structure of a perovskite oxide, e.g. $LaCuO_3$.

factors can be used to corroborate the experimental findings from the HEPO synthesis.

$$\tau = \frac{r_X}{r_B} - n_A\left(n_A - \frac{r_A/r_B}{\ln r_A/r_B}\right) \quad (2)$$

Table 1 summarizes t, μ, and τ of all compositions under investigation. The average ionic radius of the transition metals with a VI coordination was taken as r_B for the determination of these parameters.

$LaBO_3$ (B = Cr, Mn, Fe, Co, Ni, Cu, Zn) HEPOs were synthesized using metal nitrate precursors due to their solubility in water. Citric acid served as the chelating agent, while ethylene glycol was used to induce esterification during synthesis, forming a polyester network that traps metal cations to ensure homogeneity in the final product. Higher calcination temperatures are required for the synthesis of these perovskites compared to other high-entropy oxides due to the Jahn-Teller (JT) distortions arising from the inclusion of Mn in the system, which hamper the formation of a single phase.[38] As the JT distortions are favorable at lower temperatures, they help to stabilize lower-symmetry lattices, which are often multi-phase. At elevated temperatures, relaxation to the high-symmetry perovskite structures occurs because they are thermally more stable.[39]

The ideal molar configurational entropy (S_{config}) of the B-site sublattice can be estimated using **Equation (3)**, where R is the universal gas constant and x_i is the molar fraction of the i-th component.

$$S_{config} = -R\sum x_i \ln x_i \quad (3)$$

For an ideal equimolar five-cation mixture on the B-site, this simplifies to:

$$S_{config} = -R \times 5 \times 0.2\ln(0.2) = 1.61R \approx 13.4 Jmol^{-1}K^{-1}$$

Thus, the B-site sublattice reaches the commonly used high-entropy value of 1.5R. Since each targeted composition contains five equimolar B-site cations, the ideal configurational entropy is constant across the series. In contrast, the experimentally observed structural and electronic properties vary markedly with the specific cations present. This indicates that the property variations within the series are not governed by configurational entropy alone, but primarily by cation-specific enthalpic and electronic factors, including ionic-radius mismatch, electronegativity, preferred coordination geometry, oxidation-state flexibility, and Jahn–Teller activity.

Within the Gibbs free energy of mixing, $\Delta G_{mix} = \Delta H_{mix} - T\Delta S_{mix}$, the configurational entropy contribution lowers ΔG_{mix} and can therefore help stabilize otherwise unfavorable multi-cation solid solutions. At the applied calcination temperature of 1200 °C, the ideal $T\Delta S_{config}$ contribution corresponds to approximately 19.7 kJ mol^{-1}. However, the phase segregation observed for compositions containing Cu and Zn simultaneously indicates that unfavorable enthalpic contributions, arising from incompatible coordination preferences, ionic-size mismatch, and Jahn–Teller distortions, can exceed the entropic stabilization and drive phase separation. The high-entropy strategy is therefore best understood here as enabling access to a broad compositional space of La-based perovskite oxides, within which targeted cation substitutions tune structural and electronic properties, rather than as the direct mechanistic origin of all observed property changes.

Table 1
Goldschmidt tolerance factor t, octahedral factor μ, and oxidation-weighted tolerance factor τ of all compositions under investigation.

Sample name	Composition	t	μ	τ
PS-1	$La(CoCrCuFeMn)O_3$	0.970	0.436	1.686
PS-2	$La(CoCrFeMnZn)O_3$	0.952	0.465	1.688
PS-3	$La(CrCuFeMnNi)O_3$	0.971	0.435	1.683
PS-4	$La(CrFeMnNiZn)O_3$	0.952	0.464	1.686
PS-5	$La(CoCrCuMnNi)O_3$	0.975	0.43	1.676
PS-6	$La(CoCrMnNiZn)O_3$	0.956	0.459	1.678
PS-7	$La(CoCrCuFeNi)O_3$	0.975	0.43	1.676
PS-8	$La(CoCrFeNiZn)O_3$	0.956	0.459	1.678
PS-9	$La(CoCuFeMnNi)O_3$	0.972	0.434	1.682
PS-10	$La(CoFeMnNiZn)O_3$	0.953	0.463	1.684
PS-11	$La(CrCuFeMnZn)O_3$	0.958	0.455	1.732
PS-12	$La(CrCuMnNiZn)O_3$	0.962	0.449	1.713
PS-13	$La(CoCrCuNiZn)O_3$	0.966	0.444	1.700
PS-14	$La(CoCuFeNiZn)O_3$	0.963	0.448	1.711

Structural characterization

According to the X-ray diffraction (XRD) analysis of the powders in Fig. 2, all fourteen samples crystallise in either an orthorhombic or a rhombohedral structure. Similar results have been reported previously for $La(Cr_{0.2}Mn_{0.2}Fe_{0.2}Co_{0.2}Ni_{0.2})O_3$ thin films.[40] Samples PS-1 through PS-10 exhibit a pure perovskite structure, no secondary phases are detected within the resolution of XRD. In the diffraction pattern of PS-11, a secondary phase is visible, with peaks attributable to La_2O_3. In PS-12, PS-13, and PS-14, the additional weak reflections were compared with plausible secondary phases in La–Cu–Zn-containing oxide systems. The marked reflections are consistent with contributions from La_2CuO_4-type and ZnO-related secondary phases. Due to the low intensity of these reflections and partial overlap with the main perovskite peaks, a fully unambiguous assignment and quantitative phase analysis are not possible from the present laboratory XRD data alone. Nevertheless, the occurrence of these secondary reflections specifically in compositions containing both Cu and Zn supports the conclusion that the simultaneous presence of Cu and Zn destabilizes the single-phase perovskite lattice and promotes phase segregation. The observed phase segregation is consistent with the substantial ionic-radius mismatch and distinct preferred coordination geometries of Cu^{2+} and Zn^{2+}, which are known to promote local clustering and destabilize the high-entropy perovskite lattice. They also have a different preferred crystal structure ($LaZnO_3$ → hexagonal, $LaCuO_3$ → rhombohedral). Cu^{2+} exhibits pronounced JT distortions in an octahedral environment due to its d^9 configuration, creating extensive lattice strain.[41] Zn^{2+} also lacks affinity for octahedral coordination due to its d^{10} configuration, resulting in substantial enthalpic penalties when forced into the perovskite structure. The higher annealing temperature and duration can also promote the diffusion of Zn, resulting in the formation of Zn-rich phases. Furthermore, it has been observed that the segregation of Cu and Zn from a high-entropy lattice is correlated. In the $(Mg_{0.2}Co_{0.2}Ni_{0.2}Cu_{0.2}Zn_{0.2})O$ system, when Cu segregates out of the lattice, the entropic stabilization for Zn reduces, accelerating its segregation as well.[42] All of this promotes the formation of multi-phase mixtures in the presence of Cu and Zn during the synthesis of HEPOs.

Fig. 2**a** shows all the diffraction patterns of compositions that crystallise in an orthorhombic perovskite phase with a *Pnma* space group (ICSD code 70544). Fig. 2**b** shows all the diffraction patterns of compositions that crystallise in a rhombohedral perovskite phase with a *R*-3*cH* space group (ICSD code 9428). Based on the correlation between composition and resulting phase, we conclude that the simultaneous presence of Co, Ni, and Cu in the crystal leads to the formation of a rhombohedral phase. This is in accordance with the postulate that the crystal structure of the majority of the binary oxides (in this case, $LaCoO_3$, $LaNiO_3$, and $LaCuO_3$, which exhibit a rhombohedral phase) would also be forced on the high-entropy oxide. This can also be observed in the orthorhombic samples, where the presence of Cr, Mn, and Fe dominates the formation of an orthorhombic crystal. In samples with no clear majority of a preferred crystal structure in the parent phases (PS-6, PS-8, PS-10, and PS-12), the samples still tend to crystallise with an orthorhombic structure. This observation aligns with earlier predictions by Betti *et al.*, who noted that the addition of Zn in the $LaXO_3$ structure shifts the crystal structure towards an orthorhombic phase.[34]

The diffraction data were Rietveld refined to study further the crystal

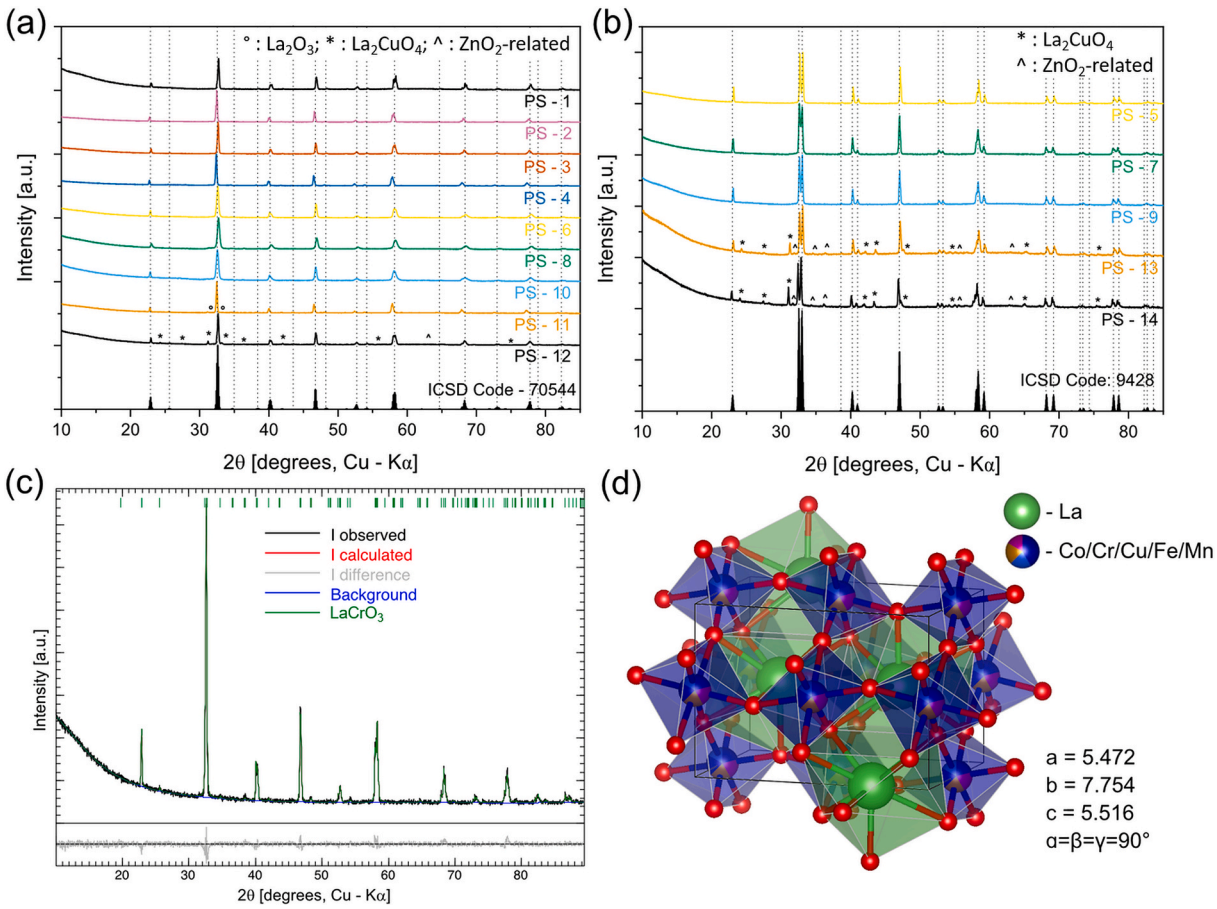

Fig. 2. (a) XRD patterns of all samples crystallizing in an orthorhombic structure. (b) XRD patterns of all samples crystallizing in a rhombohedral structure. (c) Rietveld refinement based on X-ray diffraction data of PS-1. (d) A visualization of the crystal structure of PS-1 modelled on the refinement results.

structure of the synthesized samples using the Profex software.[43] Fig. 2**c** shows the refinement for sample PS-1 (La(CoCrCuFeMn)O_3). The optimal refinement parameters ($R_{wp} = 6.11$, $R_{exp} = 5.39$, $\chi^2 = 1.2850$) were achieved with a pure phase of orthorhombic-structured oxide. Supplementary Table 1 summarizes the refinement and unit cell parameters of all other samples.

To investigate the elemental coordination of all structures, the ATR-FTIR spectra of all powder samples were recorded in the 400 – 4000 cm^{-1} range. The spectra of the samples were very similar, as shown in **Supplementary Fig. 1**. They show broad vibrations between 550 and 600 cm^{-1}, which correspond to the BO_6 octahedra and B-O bond vibrations, a characteristic feature of ABO_3 perovskites.[44] This broadening may stem from the presence of multivalent transition metals, which cause Jahn-Teller distortions, as observed strongly in $LaMnO_3$ and $LaCuO_3$, along with less pronounced distortions in the other transition metal perovskites.[45,46] Further structural distortions due to ionic size mismatch of the different cations present in the system also enhance this effect.

Morphological and Elemental Characterization

Scanning electron microscopy (SEM) was used to investigate the influence of the elemental composition on the morphology of the particles. The average particle size varies from more than 2.5 μm in PS-1 (La(CoCrCuFeMn)O_3) (Fig. 3**a**) to below 250 nm in PS-10 (La(CoFeMnNiZn)O_3) (Fig. 3**b**), while all other synthesis parameters remain constant. According to the SEM images, all samples containing Zn have smaller crystallites, and they all crystallise in the orthorhombic phase. The SEM images of all other Zn-containing samples are shown in **Supplementary** Fig. 2. This reduction in crystallite size may be attributed to local lattice distortions arising from the smaller size of the Zn^{2+} cation, which inhibits crystal growth and prevents the formation of larger crystallites.[47]

Energy-dispersive X-ray spectroscopy (EDX/EDS) mappings on all samples indicate a homogeneous and uniform distribution of all cations throughout the system at the microscale. Fig. 3**c** exemplifies the EDS mapping on a representative PS-3 (La(CrCuFeMnNi)O_3). We note that we observed similarly homogeneous distributions of the B-site elements on all other samples (data not shown here). For the single-phase compositions, EDS mapping and Rietveld refinement support homogeneous cation distribution without significant microscale segregation. For the multiphase Cu/Zn-containing samples, minor secondary phases are detected by XRD, while EDS does not indicate pronounced microscale elemental segregation within the analyzed regions.

Optical Characterization

UV–Vis-NIR spectrometry, photoelectron yield spectroscopy in air (PESA), and photoluminescence (PL) spectroscopy measurements were carried out on powders to elucidate the optoelectronic properties of the HEPOs. In particular, PESA was used to determine the ionisation potential (IP), which reflects the energetic position of the highest occupied electronic states relative to the vacuum level. In systems without a well-defined optical bandgap, the IP can be interpreted as the work-function rather than a valence-band maximum. Fig. 4**a** presents the photoelectron yield of sample PS-1 (La(CoCrCuFeMn)O_3), while the photoelectron yields of all other samples are shown in **Supplementary** Fig. 3. The IP is then determined by fitting the data. The results, summarized in Supplementary Table 2, reveal a distinct variation in IPs across the sample series, ranging from 5.17 eV (PS-9) to 5.72 eV (PS-2). This variation correlates with compositional changes: specifically, the removal of Zn from the B-site cationic sublattice decreases the IP,

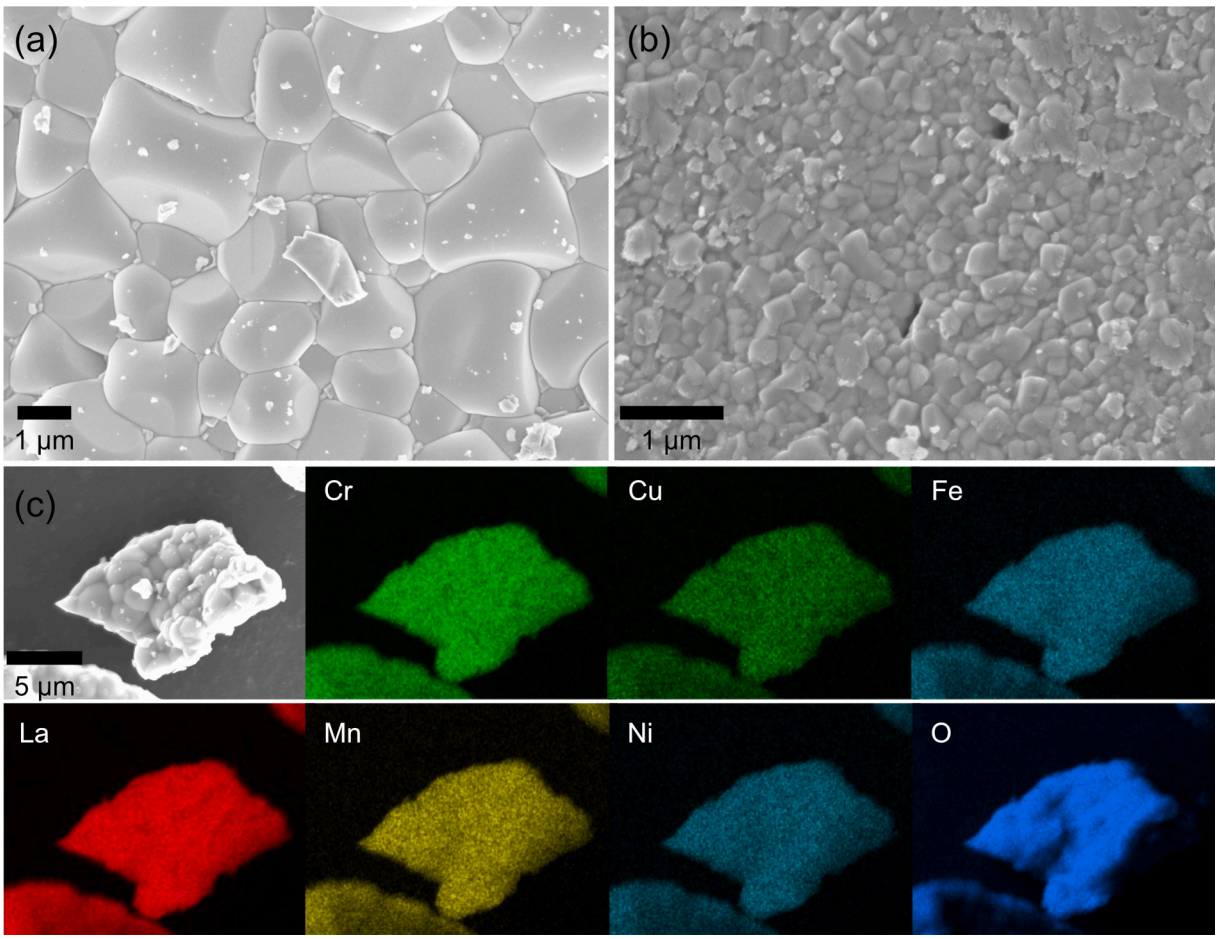

Fig. 3. (a) Representative SEM image of $La(CoCrCuFeMn)O_3$ (PS-1), i.e., without Zn. (b) Representative SEM image of $La(CoFeMnNiZn)O_3$ (PS-10), i.e., including Zn. (c) EDS mapping of $La(CrCuFeMnNi)O_3$ (PS-3).

whereas the removal of Cu increases it.

In single-B-site lanthanum transition-metal perovskite oxides, the ionisation potential has been reported to increase with increasing transition-metal electronegativity, ranging from approximately 4.3 eV for $LaCrO_3$ to 5.5 eV for $LaNiO_3$, as the transition-metal 3d states are shifted to lower energies. A similar trend can help rationalize the compositional dependence observed in the present high-entropy perovskite oxides. Zn^{2+}, with its filled d^{10} configuration, does not substantially contribute to the upper occupied states through Zn 3d–O 2p hybridization. Instead, Zn incorporation perturbs the local coordination environment and can shift the top of the occupied electronic states to lower, more strongly bound energies. Because a deeper occupied-band edge corresponds to a larger ionisation potential, Zn-containing compositions exhibit higher IP values. Conversely, removing Zn raises the occupied-band edge and thereby lowers the IP, consistent with the measured trend.[48]

In contrast, Cu^{2+}, with its d^9 configuration, contains a single hole that can be resonance-aligned with O 2p states, resulting in strong Cu 3d–O 2p hybridization near the occupied band edge. This shifts the highest occupied states upward relative to the vacuum level and therefore lowers the IP when Cu is included.[49]

These trends suggest that the electronic structure of HEPOs is highly sensitive to the presence of certain transition metals, and that the ionisation potential can be systematically tuned through compositional adjustments. This tunability is particularly relevant for tailoring energy levels in energy-conversion and catalytic systems, where interfacial energetics and charge-transfer processes play a key role. Furthermore, tuning the occupied band edge may also improve the stability under illumination.

All samples exhibit similar diffuse-reflectance behavior, indicating broadly comparable optical characteristics across the series. Fig. 4**b** shows the Tauc representation of the UV–Vis-NIR diffuse-reflectance data of PS-1 ($La(CoCrCuFeMn)O_3$), assuming an indirect electronic transition, with the corresponding diffuse-reflectance spectrum shown in the inset.[46] The optical response is broad over the full measured spectral range from 300 to 1800 nm and does not exhibit a distinct absorption onset. This suggests that the investigated HEPOs do not behave as conventional semiconductors with a sharply defined optical band edge under the applied measurement conditions.

Such broadband absorption may arise from a highly perturbed and/or strongly broadened electronic structure. One possible contribution is the hybridization between transition-metal 3d states and O 2p orbitals, particularly for late transition metals such as Ni and Cu, which can introduce electronic states close to the occupied band edge and broaden the density of states.[50–52] In addition, the compositional disorder inherent to the multi-cation B-site, together with local lattice distortions and possible oxygen-vacancy-related defect states, may further smear the density of states and obscure a sharp absorption onset. These effects can lead to a distribution of localized or weakly delocalized states rather than a single well-defined band-to-band transition.

Another possible contribution is the correlated-electron character of transition-metal oxides with partially filled d orbitals. In such systems, electron–electron interactions can split d-derived states and give rise to electronic structures that deviate from a simple semiconductor band picture.[53] Depending on the relative energetic positions of the transition-metal d states and O 2p states, the optical response may

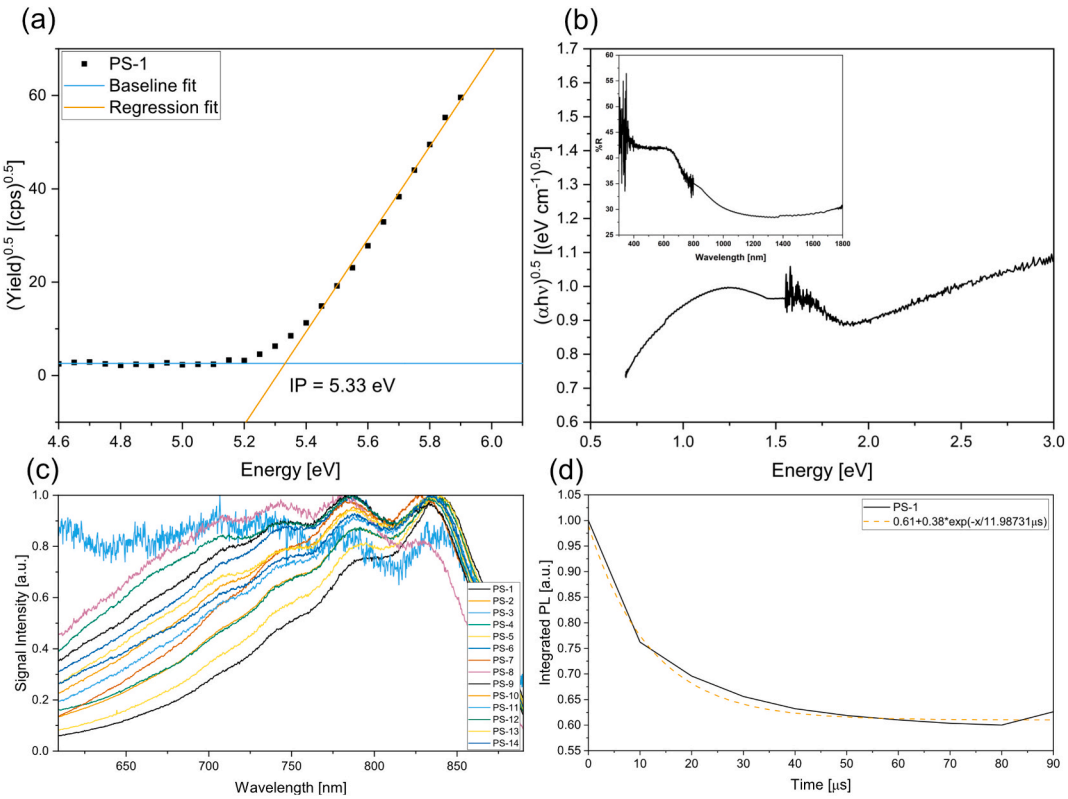

Fig. 4. (a) Fitting the PESA data of the La(CoCrCuFeMn)O_3 sample (PS-1) yields an IP of 5.33 eV. (b) Tauc representation derived from the UV–Vis-NIR diffuse-reflectance data of La(CoCrCuFeMn)O_3 (inset: UV–Vis-NIR reflectance spectrum of La(CoCrCuFeMn)O_3). (c) Normalized PL spectra of all samples. (d) Time-resolved photoluminescence decay of La(CoCrCuFeMn)O_3 (PS-1).

contain contributions with Mott-Hubbard-like or charge-transfer-like character, as discussed for related lanthanum transition-metal perovskites such as $LaMnO_3$ or $LaNiO_3$.[54] However, the present diffuse-reflectance data alone do not allow these possible contributions to be distinguished unambiguously.

Therefore, the broadband UV–Vis-NIR response is interpreted here as evidence for a strongly perturbed electronic structure in compositionally complex La-based perovskite oxides, rather than as proof of one specific microscopic mechanism. Additional temperature-dependent transport measurements, spectroscopic probes of the occupied and unoccupied density of states, such as XPS, UPS, or XAS, and electronic-structure calculations would be required to identify the dominant origin of the broadband absorption. The UV–Vis-NIR spectra of all samples under investigation are provided in **Supplementary Fig. 4**.

As shown in Fig. 4**c**, all powder samples exhibit similar photoluminescence (PL) spectra under pulsed laser excitation in a vacuum environment, with notable variations in emission intensity. The integrated PL signal scales with excitation intensity to the power of 3.6 ± 0.9, indicating a strong nonlinear response. The detector efficiency decreases at wavelengths above 850 nm, resulting in a sharp decline in the measured signal.

Interestingly, this emission vanishes entirely when the measurements are conducted in air or under a nitrogen atmosphere using the same setup. This gas-dependent behavior indicates that the emission is highly sensitive to the surrounding atmosphere. Possible contributions include enhanced thermal dissipation in the presence of gas molecules and/or atmosphere-dependent non-radiative quenching pathways. However, the present measurements do not allow the underlying mechanism to be identified unambiguously, and further atmosphere-dependent studies would be required to distinguish between thermal and electronic quenching effects.[55,56]

Fig. 4**d** presents the time-resolved emission of a representative sample PS-1 (La(CoCrCuFeMn)O_3). The extracted average lifetime of the thermal emission is (48 ± 38) µs, or (38 ± 24) µs when excluding the anomalously long decay of 143 µs observed in PS-12 (La(CrCuMnNiZn)O_3). **Supplementary Fig. 5** shows the as-measured PL spectra of all samples. Variations in laser absorption are expected due to differences in packing density, reflectivity, or surface morphology of the powder samples, which explains the observed intensity differences between samples.

To investigate the origin of the emission, the spectra were compared with the emission of a standard incandescent light bulb measured using the same optical setup, as shown in **Supplementary Fig. 6**. The incandescent lamp provides a qualitative reference for broadband thermal emission, although it does not represent an ideal black-body emitter under the present measurement conditions. The spectral shape of the HEPO emission shows a strong resemblance to this broadband thermal reference, suggesting that the observed signal is dominated by laser-induced heating rather than by conventional electronic photoluminescence. This interpretation is further supported by the nonlinear dependence of the emission intensity on excitation intensity. The integrated emission scales with excitation intensity to the power of 3.6 ± 0.9, which is broadly consistent with the temperature-dependent increase expected for thermal radiation.[57] Fits to Planck's radiation law yield effective temperatures of approximately 2450 ± 650 K under pulsed excitation. However, due to the large uncertainty of the fit, the limited spectral detection window, and the absence of a direct sample-temperature measurement, these values should be interpreted only as approximate effective temperatures rather than quantitatively determined sample temperatures.

Accordingly, the present data support an assignment to photothermal or broadband thermal-emission behavior, but they do not provide a fully conclusive or quantitative description of the emission mechanism. In particular, calibrated emissivity measurements, direct

temperature probing, and comparison with reference black-body emitters would be required to determine the absolute temperature and emissivity of the samples. Photoluminescence spectroscopy is therefore used here as a sensitive probe of laser-induced photothermal emission, rather than as evidence for conventional electronic recombination or for a fully characterized black-body emitter response.

Conclusion

A wide variety of lanthanum-based high-entropy perovskite oxides (HEPOs) with diverse transition metal compositions at the B-site were synthesized via a modified Pechini process. The use of citric acid as a chelating agent effectively ensures a homogeneous distribution of cations, which is crucial for stabilizing these complex multi-element systems. Our results demonstrate that the high-entropy approach provides a powerful lever to modulate both the crystal and electronic band structures in perovskites.

Compared with previous studies that typically investigated individual high-entropy oxide compositions or thin-film absorber systems, this work establishes a systematic link between B-site cation selection, phase stability, ionisation-potential tuning, broadband optical absorption, and photothermal response in a La-based HEPO composition series. These findings identify high-entropy perovskite oxides as a compositionally tunable platform for broadband optical absorption and photothermal behavior, while further temperature-dependent emissivity, thermal-stability, and reference-emitter measurements would be required to evaluate their suitability for specific high-temperature emitter applications.

Notably, incorporating Zn into $LaBO_3$-type perovskites provides a practical route to smaller particle sizes in HEPO powders. The crystal structure can be further fine-tuned by selecting appropriate parent perovskite templates, enabling versatile control over material properties, with the perovskite structure of the majority of binary oxides dominating the final product structure.

The ionisation potential of these HEPOs can be systematically tuned by compositional adjustments, with Cu and Zn playing key roles in decreasing or increasing the ionisation energy, respectively. The lower energy levels of the 3d orbitals of the late transition metals, combined with band broadening effects arising from the intrinsic lattice distortions induced by the high-entropy configuration, result in broadband absorption. This suggests that these materials possess either a narrow band gap or may contain contributions from Mott-Hubbard insulating behavior, opening new avenues in electronic structure engineering, but transport or spectroscopic studies are required to unambiguously distinguish these regimes. Further DFT studies would help understand the source of this bandgap narrowing. An additional intriguing feature is the observation of broadband thermal-emission behavior during photoluminescence measurements conducted under vacuum, highlighting the photothermal properties of the HEPOs. While Cu and Zn are useful for tuning the optoelectronic properties of the HEPOs, they can also promote the crystallization of a multi-phase product due to their ionic size differences and their different affinities for different coordination environments when present together in the system.

Together, these insights into the complex interplay between elemental composition, crystal structure, and optoelectronic behavior improve the rational design of next-generation functional materials. The combination of entropy-impacted crystal chemistry, tunable valence-band alignment, and strong photothermal response distinguishes HEPOs from conventional perovskites and provides a previously unexplored parameter space for optical materials engineering. These findings open the door for HEPO-based broadband photothermal oxide systems and high-temperature optical sensing platforms, a functional space not yet in the purview of conventional perovskite materials. While these materials are not conventional semiconductors, their compositionally tunable electronic structure defines a distinct functional space beyond classical optoelectronic oxides.

CRediT authorship contribution statement

Anurag Khandelwal: Writing – original draft, Methodology, Investigation, Conceptualization. **Piyush Anil Kumar Sharma:** Methodology, Investigation. **Simon Schweidler:** Writing – original draft, Supervision, Project administration, Investigation. **Pirmin Tischler:** Investigation. **Uli Lemmer:** Investigation. **Holger Röhm:** Methodology, Investigation. **Alexander Colsmann:** Supervision, Project administration, Funding acquisition. **Jasmin Aghassi-Hagmann:** Supervision, Funding acquisition. **Ben Breitung:** Writing – review & editing, Writing – original draft, Supervision, Conceptualization.

Declaration of competing interest

The authors declare that they have no known competing financial interests or personal relationships that could have appeared to influence the work reported in this paper.

Acknowledgements

A.K., P.T., U.L., H.R., A.C., and B.B. thank the Carl Zeiss Foundation for funding of the KeraSolar project. H.R. and A.C. appreciate the support from the Helmholtz research program “Materials and Technologies for the Energy Transition (MTET)”. J.A.-H. acknowledges funding by the DFG under Germany’s Excellence Strategy via the Excellence Cluster “3D Matter Made to Order” (EXC-2082/1-390761711). S. S. acknowledges funding from the German Federal Ministry of Research, Technology and Space (BMFTR) in the NanoMatFutur program within the project MAP-KAT (03XPM025).

Declaration of generative AI and AI-assisted technologies in the manuscript preparation process

During the preparation of this manuscript, the authors used ChatGPT (OpenAI) to support language editing and improve readability. All scientific content was developed by the authors, and all AI-assisted suggestions were reviewed and revised as necessary. The authors take full responsibility for the final manuscript.

Experimental section

Material synthesis

All fourteen samples were prepared using the modified Pechini process. The chemical reagents, lanthanum(III) nitrate hexahydrate, chromium(III) nitrate nonahydrate, manganese(II) nitrate tetrahydrate, iron(III) nitrate nonahydrate, cobalt(II) nitrate hexahydrate, nickel(II) nitrate hexahydrate, copper(II) nitrate trihydrate, zinc nitrate hexahydrate, anhydrous citric acid and ethylene glycol, were purchased from commercial sources (Sigma-Aldrich or Alfa-Aesar, purity $\geq$98%), and were used without further purification.

The respective metal nitrates for a given composition were dissolved in 50 mL of distilled water in stoichiometric ratios. In a separate beaker, citric acid (CA) was dissolved in ethylene glycol (EG) under constant stirring at 80 °C (molar ratio for metals: CA: EG = 1:1:4). The metal nitrate solution was added to the CA-EG solution with continuous stirring at 80 °C and stirred for ~1 hour until a homogeneous solution was obtained, signifying the formation of metal-citrate complexes. This solution was heated to 150 °C and held at this temperature for ~2 hours to induce esterification of CA with the aid of EG, thereby creating a polyester network. The metal-citrate complexes were trapped within this network, helping maintain a homogeneous distribution of cations. Water evaporated from the system on continued heating, resulting in the formation of a black viscous gel. Afterwards, the gel was pyrolyzed at 300 °C to ensure the removal of any unreacted organic precursors and moisture, until a dried ashy foam was obtained containing intermediate

metal oxides and organic complexes. The dried foam was ground in an agate mortar and pestle for 10 min with the intention of obtaining a product with a homogeneous particle size distribution. The ground gel was finally calcined in a furnace at 1200 °C under an air atmosphere, followed by slow cooling in the furnace, to obtain a fine powder. This powder was used for further characterization.

Powder X-ray diffraction

XRD (Bruker D8 diffractometer with Cu-K$\alpha_{1,2}$ radiation source) measurements were performed for the angular range of 10° – 90° with the Bragg-Brentano geometry. Rietveld refinement was done with the Profex 5.5.0 software. The refinement was carried out by modifying the elemental composition according to the respective sample, using the reference structures of $LaCrO_3$ (space group *Pnma*, code 70544) and $LaCuO_3$ (space group *R-3cH*, code 9428), taken from the ICSD database. The instrumental intensity distribution was determined by employing a reference scan of SRM-1976b (strain-free Al_2O_3 in a glassy matrix with a particle size > 2 μm).

Scanning electron microscopy

SEM measurements were performed on a ZEISS Gemini Leo 1530, equipped with an Oxford EDX detector.

Attenuated Total Reflection Infrared Spectroscopy

ATR-IR spectra were measured using a Nicolet iS50 ATR FT-IR from Thermo Scientific.

Photoelectron yield spectroscopy in air

Ionisation potentials (IPs) were determined from photoelectron yield spectroscopy (PESA) measurements of powder samples on a RIKEN KEIKI AC-2E. The photoelectron yields were corrected for the quantity of light and fitted with a power number of 0.5 to obtain the IPs. The data collected from photoelectron yield (Y) against excitation energy (hv) is fitted using a regression model, $Y = (hv\text{-}IP)^n$.

UV-Vis-NIR spectrometry

Diffuse reflectance spectra were measured using a Cary 5000 UV-Vis-NIR spectrophotometer equipped with an integrating sphere (Agilent Technologies). The as-prepared powders obtained after calcination were used directly and were not pressed into pellets. For the measurements, the loose powders were packed into optically transparent quartz spectrometer cuvettes (Starna GmbH) and placed at the reflectance port of the integrating sphere. A $BaSO_4$ reflectance standard was used for calibration.

Photoluminescence spectroscopy

The sample was illuminated with a pulsed Picolo-10 (ND:YVO_4 Laser System) from InnoLas using the frequency-tripled light with a wavelength of 355 nm. The pulse frequency is 10 kHz, and each pulse lasts 800 ps. Emitted light from the sample is led through an Acton SpectraPro SP-2300 spectrometer (Princeton Instruments) and recorded by a PI-MAX4 camera (Teledyne Princeton Instruments). All spectra are as measured and not corrected for system response.

Appendix A. Supplementary data

Supplementary data to this article can be found online at https://doi.org/10.1016/j.matdes.2026.116517.

Data availability

Data will be made available on request.

References

[1] B. Cantor, I.T.H. Chang, P. Knight, A.J.B. Vincent, Mater. Sci. Eng. A 375–377 (2004) 213.
[2] J.-W. Yeh, S.-K. Chen, S.-J. Lin, J.-Y. Gan, T.-S. Chin, T.-T. Shun, C.-H. Tsau, S.-Y. Chang, Adv. Eng. Mater. 6 (2004) 299.
[3] C.M. Rost, E. Sachet, T. Borman, A. Moballegh, E.C. Dickey, D. Hou, J.L. Jones, S. Curtarolo, J.P. Maria, Nat. Commun. (2015) 6, https://doi.org/10.1038/ncomms9485.
[4] Y. Jiang, Z. Li, T. Zhu, D. Li, H. Wang, X. Zhu, Energy Fuels 37 (2023) 9419.
[5] S. Ingavale, M. Gopalakrishnan, C.M. Enoch, C. Pornrungroj, M. Rittiruam, S. Praserthdam, A. Somwangthanaroj, K. Nootong, R. Pornprasertsuk, S. Kheawhom, Small 20 (2024) 2308443.
[6] J. Mostafaei, A. Çoruh, A. Asgari, E. Asghari, A. Niaei, J. Energy Storage 93 (2024) 112394.
[7] T.Z. Ward, R.P. Wilkerson, B.L. Musicó, A. Foley, M. Brahlek, W.J. Weber, K. E. Sickafus, A.R. Mazza, J. Phys. Mater. 7 (2024) 21001.
[8] B.L. Musicó, D. Gilbert, T.Z. Ward, K. Page, E. George, J. Yan, D. Mandrus, V. Keppens, APL Mater. 8 (2020) 40912.
[9] A. Sarkar, L. Velasco, D. Wang, Q. Wang, G. Talasila, L. De Biasi, C. Kübel, T. Brezesinski, S.S. Bhattacharya, H. Hahn, B. Breitung, Nat. Commun. (2018) 9, https://doi.org/10.1038/s41467-018-05774-5.
[10] Y. He, Y. Ting, H. Hu, T. Diemant, Y. Dai, J. Lin, S. Schweidler, G.C. Marques, H. Hahn, Y. Ma, T. Brezesinski, P.M. Kowalski, B. Breitung, J. Aghassi-Hagmann, Adv. Mater. (2025) 37, https://doi.org/10.1002/adma.202410060.
[11] L. Lin, Z. Ding, G. Karkera, T. Diemant, M.V. Kante, D. Agrawal, H. Hahn, J. Aghassi-Hagmann, M. Fichtner, B. Breitung, S. Schweidler, Small Struct. (2023) 4, https://doi.org/10.1002/sstr.202300012.
[12] S. Schweidler, M. Botros, F. Strauss, Q. Wang, Y. Ma, L. Velasco, G. Cadilha Marques, A. Sarkar, C. Kübel, H. Hahn, J. Aghassi-Hagmann, T. Brezesinski, B. Breitung, Nat. Rev. Mater. 9 (2024) 266.
[13] C. Sun, J.A. Alonso, J. Bian, Adv. Energy Mater. 11 (2021) 2000459.
[14] J. Dąbrowa, A. Olszewska, A. Falkenstein, C. Schwab, M. Szymczak, M. Zajusz, M. Moździerz, A. Mikuła, K. Zielińska, K. Berent, T. Czeppe, M. Martin, K. Świerczek, J. Mater. Chem. A 8 (2020) 24455.
[15] J. Yan, D. Wang, X. Zhang, J. Li, Q. Du, X. Liu, J. Zhang, X. Qi, J. Mater. Sci. 55 (2020) 6942.
[16] M. V. Kante, M. L. Weber, S. Ni, I. C. G. van den Bosch, E. van der Minne, L. Heymann, L. J. Falling, N. Gauquelin, M. Tsvetanova, D. M. Cunha, G. Koster, F. Gunkel, S. Nemšák, H. Hahn, L. Velasco Estrada, C. Baeumer, *ACS Nano* **2023**, *17*, 5329.
[17] H. Nan, K. Song, J. Xu, S. Lv, S. Yu, X. Hu, H. Tian, Acta Mater. 257 (2023) 119174.
[18] S. Ahmed, M.A. Gondal, A.S. Alzahrani, M. Parvaz, A. Ahmed, S. Hussain, ACS Appl. Energy Mater. 7 (2024) 1382.
[19] W.-J. Yin, B. Weng, J. Ge, Q. Sun, Z. Li, Y. Yan, Energy Environ. Sci. 12 (2019) 442.
[20] J. Ma, T. Liu, W. Ye, Q. He, K. Chen, J. Energy Storage 90 (2024) 111890.
[21] P. Zhang, Y. Shi, Y. Zhang, S. Feng, L. Shi, J. Pan, J. Cao, C. Li, Chem. Eng. J. 487 (2024) 150727.
[22] W. Bao, H. Shen, Y. Zhang, C. Qian, G. Zeng, K. Jing, D. Cui, J. Xia, H. Liu, C. Guo, F. Yu, K. Sun, J. Li, J. Mater. Chem. A 12 (2024) 23179.
[23] M. Kumbhakar, A. Khandelwal, S.K. Jha, M.V. Kante, P. Keßler, U. Lemmer, H. Hahn, J. Aghassi-Hagmann, A. Colsmann, B. Breitung, L. Velasco, S. Schweidler, Adv. Energy Mater. 13 (2023) 2204337.
[24] M. Fracchia, M. Coduri, P. Ghigna, U. Anselmi-Tamburini, J. Eur. Ceram. Soc. 44 (2024) 585.
[25] J.V. Patil, S.S. Mali, C.K. Hong, Adv. Funct. Mater. 35 (2025) 2408721.
[26] S. Schweidler, Y. Tang, L. Lin, G. Karkera, A. Alsawaf, L. Bernadet, B. Breitung, H. Hahn, M. Fichtner, A. Tarancón, M. Botros, Front. Energy Res. (2022) 10, https://doi.org/10.3389/fenrg.2022.983979.
[27] C. Xie, H. Miao, F. Wan, Y. Wang, D. Li, R. Liu, J. Am. Ceram. Soc. 107 (2024) 5105.
[28] L. Dimesso, in *Handb. Sol-Gel Sci. Technol.* (Eds.: L. Klein, M. Aparicio, A. Jitianu), Springer International Publishing, Cham, **2016**, pp. 1–22.
[29] A. Khandelwal, G. Mathew, S. Bhattacharya, A. Colsmann, G.C. Marques, M. Botros, F. Strauss, J. Xing, J.S. Raju, A. Ponnusamy, J. Aghassi-Hagmann, T. Brezesinski, S. Schweidler, B. Breitung, Small 21 (2025) e01703.
[30] R. Kundu, Adv. Theory Simul. (2025) e01186.
[31] M.K. Hossain, A.A. Arnab, D.P. Samajdar, M.H.K. Rubel, M.M. Hossain, M.R. Islam, R.C. Das, H. Bencherif, M.F. Rahman, J. Madan, R. Pandey, S. Bhattarai, M. Amami, D.K. Dwivedi, Energy Fuels 37 (2023) 13377.
[32] S. Baruah, J. Borah, S. Maity, Sol. Energy 280 (2024) 112858.
[33] R. Sa, B. Luo, Z. Ma, L. Liang, D. Liu, J. Solid State Chem. 309 (2022) 122956.
[34] L. Angelo Betti, L. Rita Magnaghi, A. Bosetti, R. Biesuz, L. Malavasi, J. Mater. Chem. C 12 (2024) 7695.
[35] J.A. Dias, M.A.S. Andrade, H.L.S. Santos, M.R. Morelli, L.H. Mascaro, ChemElectroChem 7 (2020) 3173.
[36] V.M. Goldschmidt, Naturwissenschaften 14 (1926) 477.
[37] C. Li, K.C.K. Soh, P. Wu, J. Alloys Compd. 372 (2004) 40.
[38] C. Oses, C. Toher, S. Curtarolo, Nat. Rev. Mater. 5 (2020) 295.
[39] M.A. Awad, A.M. Rayan, I.A. Abdel-Latif, M.R. Ahmed, Sci. Rep. 15 (2025) 29514.

[40] M. Brahlek, A.R. Mazza, K.C. Pitike, E. Skoropata, J. Lapano, G. Eres, V.R. Cooper, T.Z. Ward, Phys. Rev. Mater. 4 (2020) 54407.
[41] J.M. Gallmetzer, F.R.S. Purtscher, J. Gamper, A. Mohammadi, R. Feyerherm, W. Riedel, S. Penner, T.S. Hofer, J. Phys. Chem. C 129 (2025) 677.
[42] M. Webb, M. Gerhart, S. Baksa, S. Gelin, A.-R. Ansbro, P.B. Meisenheimer, T. Chiang, J.-P. Maria, I. Dabo, C.M. Rost, J.T. Heron, Appl. Phys. Lett. 124 (2024) 151904.
[43] N. Doebelin, R. Kleeberg, J. Appl. Crystallogr. 48 (2015) 1573.
[44] P. Sfirloaga, M. Poienar, I. Malaescu, A. Lungu, P. Vlazan, J. Rare Earths 36 (2018) 499.
[45] A. Sarkar, R. Djenadic, D. Wang, C. Hein, R. Kautenburger, O. Clemens, H. Hahn, J. Eur. Ceram. Soc. 38 (2018) 2318.
[46] N. Hamada, H. Sawada, I. Solovyev, K. Terakura, Phys. B Condens. Matter 237–238 (1997) 11.
[47] K. Ambujam, A. Sridevi, S. Pandiaraj, A.N. Alodhayb, Mater. Sci. Eng. B 308 (2024) 117617.
[48] L.Y. Lim, S. Lany, Y.J. Chang, E. Rotenberg, A. Zunger, M.F. Toney, Phys. Rev. B 86 (2012) 235113.
[49] T. Tabari, M. Kobielusz, D. Singh, J. Yu, W. Macyk, ACS Appl. Eng. Mater. 1 (2023) 2207.
[50] G. Gou, I. Grinberg, A.M. Rappe, J.M. Rondinelli, Phys. Rev. B (2011) 84, https://doi.org/10.1103/physrevb.84.144101.
[51] W. Shi, J. Zhang, B. Yu, J. Zheng, M. Wang, Z. Li, J. Zheng, B. Liu, Y. Chen, F. Hu, B. Shen, Y. Chen, J. Sun, Nat. Commun. (2024) 15, https://doi.org/10.1038/s41467-024-54311-0.
[52] C.-Y. Liu, L. Celiberti, R. Decker, K. Ruotsalainen, K. Siewierska, M. Kusch, R.-P. Wang, D.J. Kim, I.I. Olaniyan, D. Di Castro, K. Tomiyasu, E. Van Der Minne, Y. A. Birkhölzer, E.M. Kiens, I.C.G. Van Den Bosch, K.N. Patil, C. Baeumer, G. Koster, M. Lazemi, F.M.F. De Groot, C. Dubourdieu, C. Franchini, A. Föhlisch, Commun. Phys. (2024) 7, https://doi.org/10.1038/s42005-024-01642-5.
[53] J. Klein, L. Kampermann, B. Mockenhaupt, M. Behrens, J. Strunk, G. Bacher, Adv. Funct. Mater. (2023) 33, https://doi.org/10.1002/adfm.202304523.
[54] H. Wang, Q. Zhang, M. Qiu, B. Hu, J. Mol. Liq. 334 (2021) 116029.
[55] W. Jaimes Salcedo, F.J. Ramirez Fernandez, J.C. Rubim, Spectrochim. Acta. A. Mol. Biomol. Spectrosc. 60 (2004) 1065.
[56] R. Lin, S. Liu, J. Ye, X. Li, J. Zhang, Adv. Sci. 3 (2016) 1500434.
[57] L. Boltzmann, Ann. Phys. 258 (1884) 291.